

Thermodynamic Transferability in Coarse-Grained Force Fields using Graph Neural Networks

Emily Shinkle,^{*,†} Aleksandra Pachalieva,^{‡,¶} Riti Bahl,^{§,||} Sakib Matin,^{||} Brendan Gifford,^{||} Galen T. Craven,^{||} and Nicholas Lubbers^{*,†}

[†]*Computer, Computational, and Statistical Sciences Division, Los Alamos National Laboratory, Los Alamos, NM 87545, USA*

[‡]*Earth and Environmental Sciences Division, Los Alamos National Laboratory, Los Alamos, NM 87545, USA*

[¶]*Center for Nonlinear Studies, Los Alamos National Laboratory, Los Alamos, NM 87545, USA*

[§]*Department of Mathematics, Emory University, Atlanta, GA 30322*

^{||}*Theoretical Division, Los Alamos National Laboratory, Los Alamos, NM 87545, USA*

E-mail: eshinkle@lanl.gov; nlubbers@lanl.gov

Abstract

Coarse-graining is a molecular modeling technique in which an atomistic system is represented in a simplified fashion that retains the most significant system features that contribute to a target output, while removing the degrees of freedom that are less relevant. This reduction in model complexity allows coarse-grained molecular simulations to reach increased spatial and temporal scales compared to corresponding all-atom models. A core challenge in coarse-graining is to construct a force field that represents the interactions in the new representation in a way that preserves the atomistic-level properties. Many approaches to building coarse-grained force fields have

limited transferability between different thermodynamic conditions as a result of averaging over internal fluctuations at a specific thermodynamic state point. Here, we use a graph-convolutional neural network architecture, the Hierarchically Interacting Particle Neural Network with Tensor Sensitivity (HIP-NN-TS), to develop a highly automated training pipeline for coarse grained force fields which allows for studying the transferability of coarse-grained models based on the force-matching approach. We show that this approach not only yields highly accurate force fields, but also that these force fields are more transferable through a variety of thermodynamic conditions. These results illustrate the potential of machine learning techniques such as graph neural networks to improve the construction of transferable coarse-grained force fields.

Introduction

Molecular simulations elucidate the microscopic physical processes that give rise to a physical system’s function and behavior. One of the principal components that determines the accuracy of a molecular simulation is the force field, a mathematical model that calculates the forces acting on the particles in the system as a function of their positions, i.e., the interatomic forces. Force fields are typically constructed and calibrated by a combination of top-down parameterization techniques (so that a simulation reproduces known properties of the target system such as structural, thermodynamic, and dynamical properties measured in experiments) and bottom-up techniques (by fitting to forces generated using first-principles calculations¹⁻⁶). Molecular models with well-parameterized force fields enable the determination of key physical and chemical properties needed by researchers in a variety of domains such as chemistry, materials science, and biophysics.^{3,7-9} These properties are generated by extracting observable quantities from the results of a simulation using a variety of sampling techniques.^{10,11}

Even with a force field in hand, performing molecular simulations can incur a significant computational cost, primarily because large numbers of atoms are often required in

order to understand a system’s collective behaviors and statistical properties. To ameliorate the computational cost associated with simulating a system at an all-atom (AA) level, the system can be redefined using a coarse-grained (CG) representation in which some of the atomistic degrees of freedom are removed to reduce the overall model complexity. Specifically, coarse-graining is a molecular modeling technique in which collections of atoms with highly interrelated behavior are reduced to single particles.^{1,12–23} By neglecting and removing the internal dynamics of the atoms within each group, CG models increase computational efficiency and allow simulations to be performed over increased spatial and temporal scales. Coarse-graining has been shown to be capable of reproducing the structural and thermodynamic properties of a broad class of systems including molecular liquids,^{1,24–27} polymers,^{28–31} and proteins.^{9,12,13,15}

A limitation of traditional coarse-graining techniques and the corresponding force fields used to perform the CG simulations is transferability – that is, CG models are optimized at a specific thermodynamic state point, but perform poorly outside of those conditions.³² The transferability problem arises because the effects of the removed degrees of freedom are themselves a function of thermodynamic conditions.³³ Researchers are attempting to tackle the transferability problem using a variety of techniques, including inverse Monte Carlo methods,³⁴ extended ensemble approaches^{35,36} and integral equation methods,³⁷ among others. A related approach is to use thermodynamic consistency^{38–40} to provide data-driven models across thermodynamic conditions.

The development of AA and CG force fields is a complex task that involves selection of functional forms, creation and curation of data, optimization of parameters, evaluation of preliminary models, and tuning of hyper-parameters (such as cost functions weights) associated with fitting.⁴¹ Recently, approaches using machine learning (ML) methods have been applied to build many-body models of atomistic^{3,7,8,42,43} and coarse-grained^{31,44–46} forces with increased flexibility in comparison to traditional methods. These approaches allow for tight matching with reference data, but introduce even more hyper-parameters to the model

and fitting procedure, further complexifying the automation of force field development.

In this paper, we present an ML CG workflow to construct force fields based on the force-matching (or multi-scale coarse-graining) approach⁴⁷ using the Hierarchically Interacting Particle Neural Network with Tensor Sensitivity (HIP-NN-TS)^{48,49} architecture, which has previously only been applied to AA systems. We show that this workflow is robust in that it is able to consistently build a large number of accurate CG models for a variety of chemical physics systems across many thermodynamic state points. We then use these models to study transferability of the many-body ML CG approach. We compare these results to two-body effective potentials using the recently developed OpenMSCG⁵⁰ software. We find that the ML CG approach is more consistently accurate, can take advantage of additional training data, and produces more transferable models across varying temperature. We furthermore study several molecules across temperature and density variations, comparing single-state-point models with models produced by training to all available data, and find that both types are surprisingly transferable even as systems undergo large changes in their structural ordering.

Methods

In this section, we describe training data generation, the ML model architecture, the training procedure, and evaluation methods used in this work. An overview of the workflow is shown in Figure 1.

Coarse-graining

We use a typical coarse-graining framework in which collections of atoms in an AA system are mapped to CG *beads* and internal degrees of freedom in each collection of atoms are removed from the CG model. With this aim, a mapping from the AA configuration space to the CG resolution is selected. We use a bottom-up approach to construct the corresponding

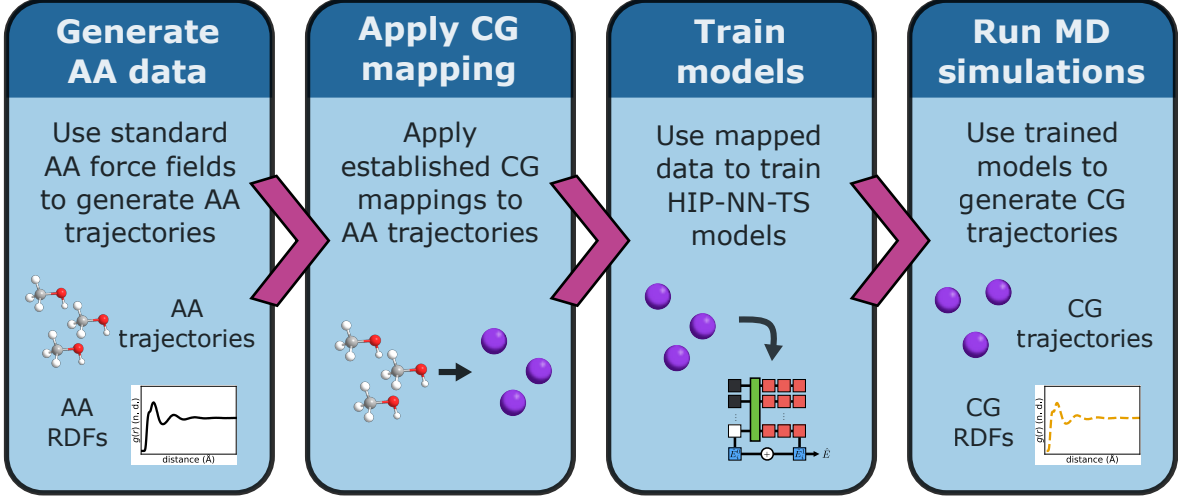


Figure 1: An illustration of the workflow used to create and analyze the ML CG models

CG force field, which is defined to preserve the configuration probability density from the AA space in the CG space.⁵¹ The relation between the configuration probabilities in each representation is

$$P_{CG}(\mathbf{R}) = \int P_{AA}(\mathbf{r})\delta[\mathcal{M}(\mathbf{r}) - \mathbf{R}] d\mathbf{r}, \quad (1)$$

where $\mathbf{r} = \{\mathbf{r}_1, \mathbf{r}_2, \dots, \mathbf{r}_n\}$ represents the positions \mathbf{r}_i for atoms $1 \leq i \leq n$ in the AA space, $\mathbf{R} = \{\mathbf{R}_1, \mathbf{R}_2, \dots, \mathbf{R}_N\}$ the positions \mathbf{R}_I for CG beads $1 \leq I \leq N$, \mathcal{M} the mapping function from \mathbf{r} to \mathbf{R} , and P_{CG} and P_{AA} the respective CG and AA configuration probability densities. For the canonical ensemble generated by an AA energy E_{AA} at inverse temperature β , this equation can be cast in terms of a *free energy function* E_{CG} as

$$e^{-\beta E_{CG}(\mathbf{R})} \propto \int e^{-\beta E_{AA}(\mathbf{r})}\delta[\mathcal{M}(\mathbf{r}) - \mathbf{R}] d\mathbf{r}. \quad (2)$$

This free energy function is a *potential of mean force*, in that the CG forces derived from it should match the force averages across all possible atomistic configurations corresponding to each CG configuration, based on the selected mapping \mathcal{M} .

Herein each CG bead represents the atoms that compose a single molecule, and we invoke a center-of-mass mapping to construct the CG representation. We define the mass M_I of a

bead I as a sum of the masses m_i for each atom i in the corresponding molecule as

$$M_I = \sum_{i=1}^n m_i \Delta_{i,I}, \quad (3)$$

where Δ is an indicator for which atoms correspond to which bead,

$$\Delta_{i,I} = \begin{cases} 1, & \text{atom } i \text{ is in molecule } I, \\ 0, & \text{otherwise.} \end{cases} \quad (4)$$

The dynamical variable in the coarse-grained model we use is the center of mass position, \mathbf{R}_I , i.e.

$$\mathbf{R}_I = \mathcal{M}(\mathbf{r})_I = \frac{\sum_{i=1}^n m_i \mathbf{r}_i \Delta_{i,I}}{M_I}. \quad (5)$$

Also required is a mapping \mathcal{B} from AA forces $\mathbf{f} = \{\mathbf{f}_1, \mathbf{f}_2, \dots, \mathbf{f}_n\}$ to CG forces $\mathbf{F} = \{\mathbf{F}_1, \mathbf{F}_2, \dots, \mathbf{F}_N\}$. Ciccotti, Kapral, and Vanden-Eijnden⁵² derived a set of criteria for \mathcal{B} that guarantees that the corresponding free energy function E_{CG} is consistent with equation 1. Summarily, while \mathcal{B} may be nonlinear in \mathbf{r} , it must be linear in \mathbf{f} , and \mathcal{B} must serve as an inverse of the AA gradient of the coordinate mapping, $\nabla_{\mathbf{r}} \mathcal{M}$, when contracted over the AA indices. A simple choice consistent with this criteria is to define \mathcal{B} so that \mathbf{F}_I is the sum of forces \mathbf{f}_i for atoms i in bead I , i.e.

$$\mathbf{F}_I = \mathcal{B}(\mathbf{f})_I = \sum_{i=1}^n \mathbf{f}_i \Delta_{i,I}. \quad (6)$$

Using these CG mappings, for each frame of data, \mathbf{F} provides an unbiased estimator of the negative derivative of the CG free energy E_{CG} with respect to the coordinates \mathbf{R} .

Model architecture

To build the CG free energy function E_{CG} , we applied the Hierarchically Interacting Particle Neural Network with Tensor Sensitivity (HIP-NN-TS).⁴⁹ HIP-NN-TS is a graph-convolutional

neural network (GCNN); the convolutions, implemented in an *interaction layer*, make the model invariant under rotations, translations, and permutations of the atoms in the simulation. The tensor-sensitivity component builds upon the original model⁴⁸ by introducing many-body features into the individual neurons of the interaction layer.

We adapted the open-source `hippynn`⁴⁸ codebase that implements HIP-NN-TS to take bead positions as inputs rather than atom positions. The models then predict the free energy of the system based on the bead configurations. The force on each bead is calculated as the negative gradient of the predicted free energy with respect to the bead positions using automatic differentiation.⁵³ Using the language of Ref. 49, the ML CG models developed here use tensor order $\ell = 2$ and contain $n_{\text{int}} = 1$ interaction layer, $n_{\text{atom}} = 3$ atomic environment layers, $n_{\nu} = 20$ sensitivity functions, and $n_{\text{feature}} = 32$ atomic features per layer.

In addition to the neural network component of the free energy, a short-ranged pairwise repulsive potential was added to the models. The data used to train the models comes from equilibrium simulations in which there is an effective lower bound on intermolecular distance, r . Without the addition of the repulsive potential, the models can generate unphysical, untrained predictions for the forces between pairs of beads whose distance is less than r , due to the lack of data. The repulsive potential ensures that any two beads separated by less than r are repelled, as implied by the lack of data for that region of phase space. The repulsive potential is of the form

$$E_{\text{rep}}(r) = E_0 e^{-ar} \tag{7}$$

where r is the distance between the pair of beads, and $E_0, a > 0$ are parameters set based on the specific system. Importantly, because the pairwise potential pertains to lack of data, it is necessary to set E_0 and a before training the neural network. The procedure used for identifying E_0 and a is detailed in the Supporting Information. We emphasize that the repulsive pair potential significantly improves the stability of learned ML CG models during simulations, resulting in a highly automated workflow.

Training

For the methanol comparison study, we follow the data generation scheme described in an OpenMSCG tutorial⁵⁴ for building CG models of methanol. The molecular dynamics suite GROMACS⁵⁵ is used to generate 100,000 timesteps of 1 fs each of a box with 1,728 methanol molecules under periodic boundary conditions. Every 100th step is saved, resulting in 1,000 AA frames. The topology and initial coordinates are downloaded from the GROMACS webpage and the OPLS-AA⁵⁶ force field is used. The simulation is run in the canonical ensemble using a Nosé-Hoover thermostat.

For the cross-molecular study, we use the LAMMPS⁵⁷ software package with the GROMOS-54A7⁵⁸ force field to simulate three molecular fluids: methanol, benzene, and methane across a variety of temperatures and densities above the critical temperature for each molecule. The molecular topologies were obtained using the Automated Topology Builder (ATB) and Repository.^{59,60} PACKMOL⁶¹ was used to generate initial coordinates and Moltemplate⁶² was used to generate PACKMOL input files. We performed MD simulations in the canonical ensemble using a Nosé-Hoover thermostat. Each simulation contained 1,024 molecules and the density was controlled using cubic boxes of various size with periodic boundary conditions. Following an equilibration procedure, each MD simulation consisted of 50,000 timesteps of 1 fs. Every 50th frame was recorded, totalling 1000 frames.

For both studies, after generating the AA data, the mappings \mathcal{M} of Eq. 5 and \mathcal{B} of Eq. 6 were applied to each frame to create the training data for the ML CG models. For the methanol comparison study and the cross-molecular study, we trained *single-state* models using data from a single state point (i.e. for each temperature and density combination). These single-state models are then applied using MD at the same state point to which they were trained to establish a baseline. They are also applied with MD at other temperatures and densities, to test their transferability. For the cross-molecular study, we also trained a *multi-state* model for each molecule using combined data from every state point and tested it using MD at each of those state points. See Figure 2 for an illustration of these three

different test schemes.

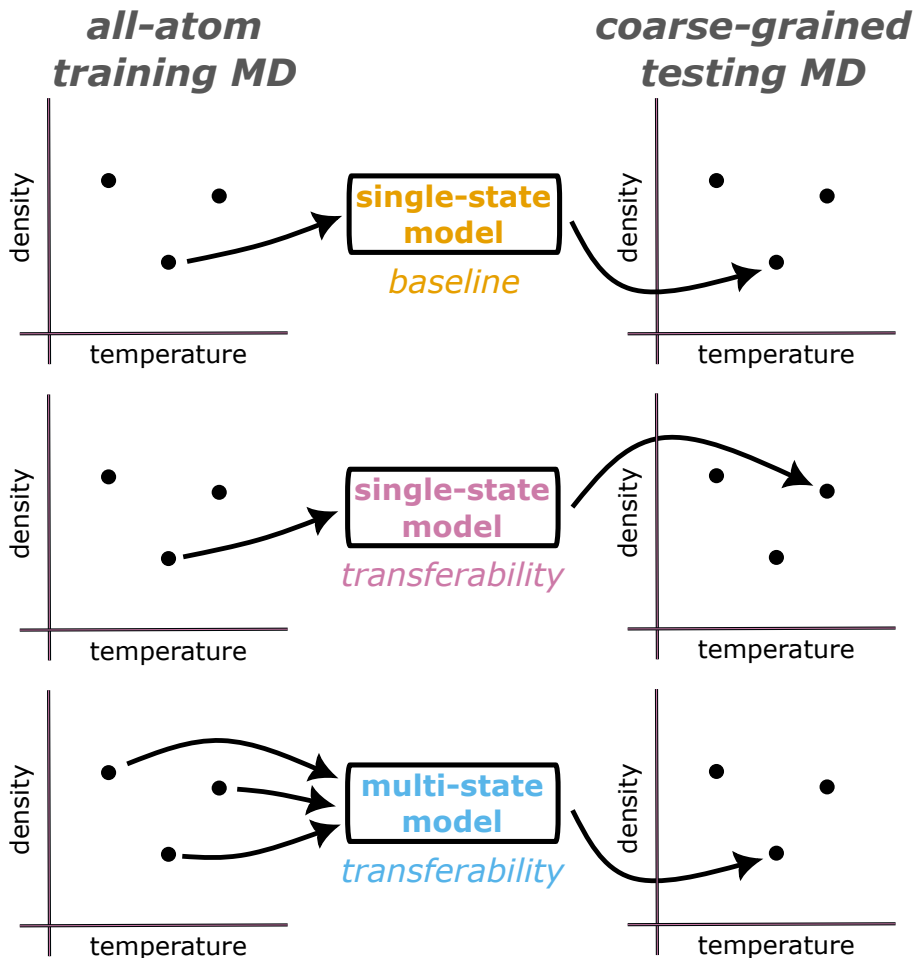


Figure 2: An illustration of the three types of tests performed on the ML CG method.

The multi-state datasets are the same size as the single-state datasets, built by evenly subselecting the frames from each state point. In each case, the 1000 frames of training data are split randomly into 800 training frames, 100 validation frames, and 100 testing frames. The loss function used to train the ML CG models was the sum of the root mean square error (RMSE) and mean absolute error (MAE) for the model predictions versus the training data values of the forces for each configuration in the dataset.

Performance evaluation

We measure the accuracy of CG models by how well they reproduce statistics from the AA models, in accordance with Eq. 1. In particular, the radial distribution functions (RDFs) measured during MD simulations using the CG models were compared to the RDFs generated from the AA MD simulations. The RDF, denoted by $g(r)$, describes the statistics for finding a particle at distance r from a randomly chosen particle. It is normalized so that an RDF is asymptotically one for large radii by defining the RDF as the ratio between the local density variations and the bulk density.⁶³ The RDF is a key structural metric used in characterizing the degree of local ordering in a system. It can be determined using theoretical, computational, or experimental approaches, and can be used to derive much thermodynamic information about a system.⁶³⁻⁶⁷ In this work, AA RDFs are computed using molecular centers of mass, and CG RDFs, correspondingly, are computed using the bead positions.

In order to construct the CG RDFs, we performed CG MD simulations in the canonical ensemble. The initial positions for these simulations were taken from a random frame of the model training data at the appropriate temperature and density. After equilibrating the CG system, 50,000 timesteps of 1 fs each were run, and each 50th frame was recorded. The RDFs were computed from these 1,000 frames of data. The AA RDFs were taken from the AA training data, which was also performed using canonical ensemble MD as detailed in the Training subsection.

To quantify the difference AA and CG RDFs, we use the *total absolute error* (TAE). The TAE is the total area between two curves, i.e.,

$$\text{TAE}(g_1, g_2) = \int_0^\infty |g_2 - g_1| dr. \tag{8}$$

For the calculations in this paper, we used a finite sum approximation of TAE. Specifically,

we used

$$\text{TAE}(g_1, g_2) \approx \sum_{i=0}^n |g_2(r_i) - g_1(r_i)| \Delta_r, \quad (9)$$

where $\{r_j\}$ represents a sequence of distance values, evenly spaced between $r_0 = 0$ and an appropriately chosen $r_n = r_{\max} > 0$, with width Δ_r between each pair of successive values. We chose TAE to compare RDFs rather than MAE because the TAE is not strongly sensitive to the choice of upper cutoff r_{\max} of the RDF radius, whereas the MAE is.

A usual method for evaluating ML models is to examine error metrics such as MAE and RMSE on test data reserved from training. However, for the CG problem here, the training data \mathbf{F} is a statistical distribution of forces, whereas the model predicts the mean of this distribution, $\langle \mathbf{F} \rangle$; as a result, there is intrinsic noise in the loss function.⁶⁸ For this reason, conventional metrics are not easily usable for assessing the quality of the ML CG model. Nevertheless, several conventional metrics for the performance of the models are reported in the Supporting Information, and we do observe that within a given problem, there is some correspondence between the error given by RDF TAE and by force MAE/RMSE.

Results

In this section, the performance of the ML CG models is explored. Both *single-state* models, those trained using data at a specific temperature and density, and *multi-state* models, those trained using data from a range of temperatures and densities, are discussed.

Methanol Comparison Study

To establish a baseline for the ML CG approach, we compared it to the recently released OpenMSCG software for coarse-graining methanol.⁵⁰ OpenMSCG is based upon methods proposed by Izvekov and Voth^{1,69} and later further developed and generalized by others including Noid et. al.^{47,51,70} The OpenMSCG software provides a set of *force-matching* routines which implement a bottom-up coarse-graining method that calculates the effective CG

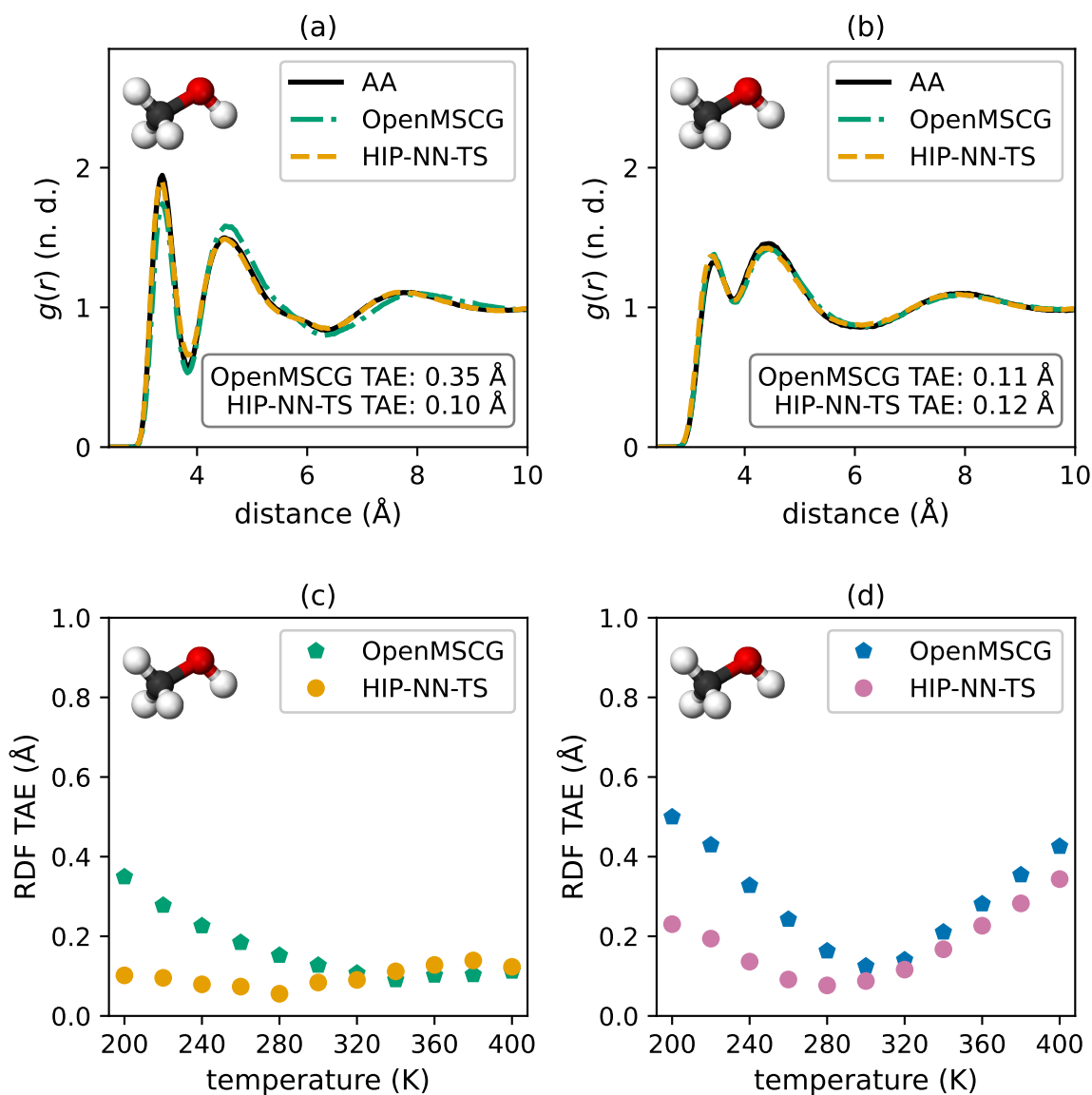


Figure 3: Subfigures (a) and (b) show a comparison of methanol RDFs generated using (1) a reference AA simulation, (2) the MS-CG technique, and (3) the single-state ML CG models. These RDFs were generated at (a) 200 K, density 0.77 g/cm^3 and (b) 400 K, density 0.77 g/cm^3 . Subfigure (c) summarizes the corresponding results across 11 temperatures. Subfigure (d) shows the transferability of a single-state model for each method, each trained with 300 K data.

interactions by minimizing the difference between CG forces and reference AA forces; this is quite similar to our workflow and uses the same coordinate and force mappings. The main difference is that OpenMSCG uses a pairwise force/energy function between beads instead of a GCNN.

The results of this comparison are given in Fig. 3. Both methods perform well, with the ML CG method exhibiting significantly lower error at lower temperatures as shown in Figure 3(a) for 200K. These results illustrate that, in general, we expect the neural network-based methodology to result in CG force fields that perform as well as or better than those constructed using force-matching when applied to data at a specific state point. Figure 3(b) shows results for methanol at 400 K. In this case, the OpenMSCG and ML CG methods give very similar and excellent overall accuracy. As such, in this case, there is only a limited potential for improvement over the OpenMSCG model. We performed this study for a range of temperatures from 200K to 400K, with the overall RDF TAEs presented in Figure 3(c). At lower temperatures, the ML CG models perform substantially better than the OpenMSCG models. As the the temperature is increased, the difference between the two methods is less pronounced. In the temperature range 340K-380K, the OpenMSCG method is slightly more accurate, although the difference between the methods is relatively small. The models shown in Figure 3(c) were trained using 1000 frames of training data. In the SI Figure S1, we show similar results constructed using 10 and 100 frames of training data. With far fewer data, the advantage of ML CG over OpenMSCG is less pronounced; we find the performance of OpenMSCG saturates more quickly as the dataset size is increased.

To understand the transferability of the models, we applied the single-state model learned at 300K for each method to a range of temperatures and recorded the TAEs of the resulting trajectories in Figure 3(d). In both cases, the model produces lower errors in the vicinity of the training state point, and the TAE rises smoothly at higher and lower temperatures. However, the ML CG model shows significant lower TAE compared to OpenMSCG when applied at temperatures further from the training state point. At temperatures lower than

300 K, the TAE of ML CG is approximately a factor 2 lower in comparison to OpenMSCG. As the main difference in the methods is the many-body nature of the ML CG model vs. the pairwise nature of OpenMSCG, this illustrates how accounting for many-body interactions may be relevant to producing more transferable CG force fields.

Cross-molecular Study

To further study thermodynamic transferability in ML CG models, we applied the ML CG method to several molecules (methanol, benzene, and methane) across a range of temperatures and densities as described in the Training subsection.

Figure 4 shows examples of the RDFs generated using single-state models for methanol, benzene, and methane. Each subfigure shows a reference AA RDF computed using molecular centers-of-mass for atomistic MD data generated at the same temperature and density. There is excellent agreement between the AA and CG RDFs in each case, illustrating that the ML CG models accurately capture the shape and magnitude of the RDF peaks for each of the examined molecular fluids.

Figure 5 shows the results of three workflows for all three molecules studied across the nine state points used for each molecule. First, the single-state models are used to provide a baseline of a usual CG approach which trains and tests at the same thermodynamic state point (denoted *single-state (base.)* in the figure). Second, for each molecule, the single-state model trained at the center state point is applied to each of the test state points (denoted *single-state (trans.)*), providing a picture of the transferability of the ML CG model when extrapolating through thermodynamic state space. Finally, the multi-state model is applied to each state point (denoted *multi-state (trans.)*) to test whether training to all state points provides improved transferability characteristics (for details see the Training section). Each molecular fluid was studied at three densities (shown in three panels) and three temperatures (shown on the vertical axis of each panel) in Figure 5. The error bars show the standard deviation calculated across five trials, where in each trial, several factors were randomly

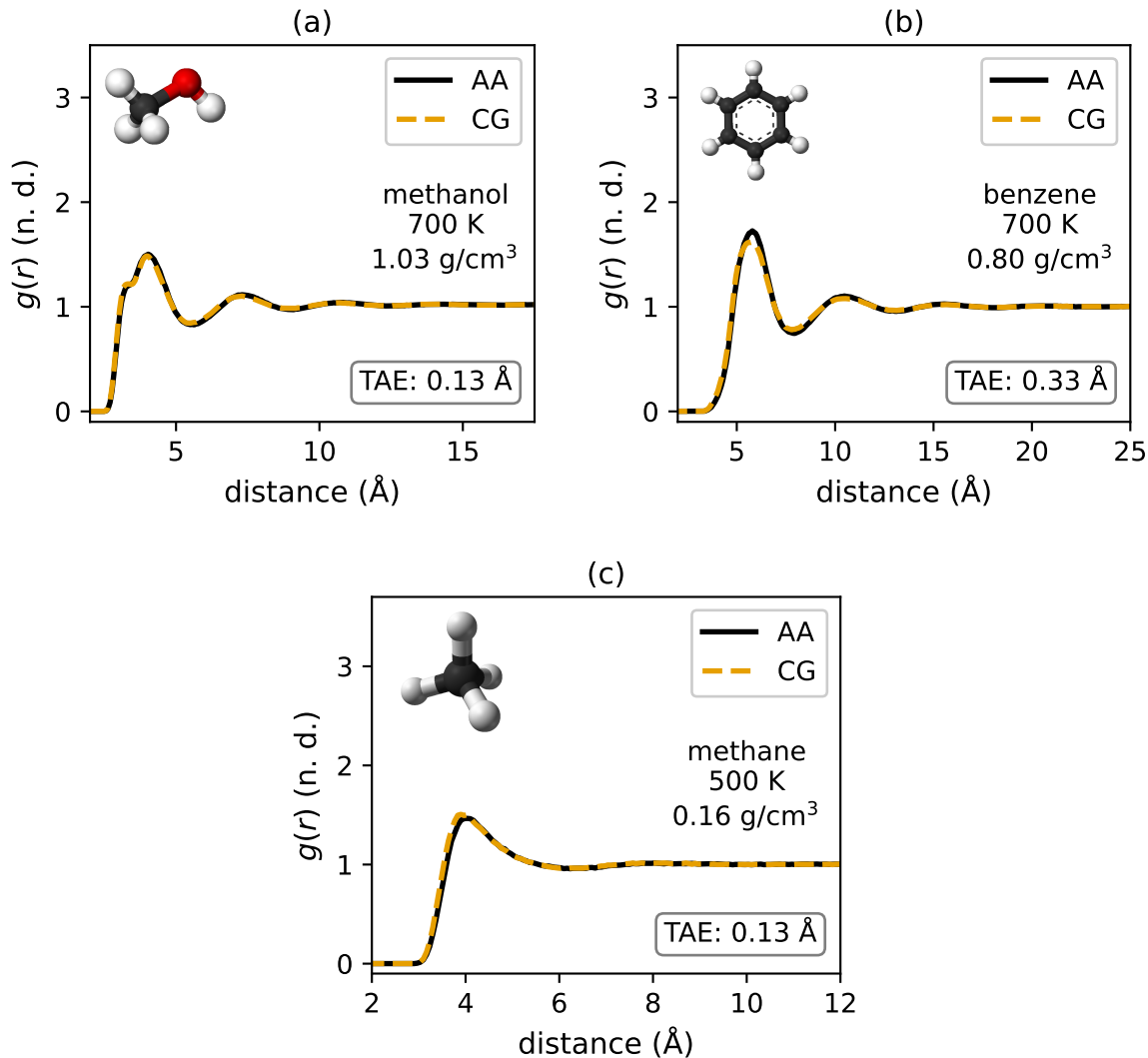


Figure 4: Baseline comparison of reference RDFs generated from AA MD against RDFs generated via a ML CG single-state model for (a) methanol, (b) benzene, and (c) methane.

varied: the train/valid/test split for the data used to create the ML CG model, the initial weights of the HIP-NN-TS network, the initial frame for the ML CG dynamics, and the random number seed used for the thermostat.

The findings for the single-state baseline test were consistent for the three molecules. For methanol (Figure 5(a)), we observe that the single-state models generate similar, very low (< 0.25 Å) TAE values over all the densities and temperatures studied. For benzene (Figure 5(b)), the average TAE is good (< 0.45), although somewhat higher than methanol, but again, single-state models produce fairly consistent TAE values across all state points.

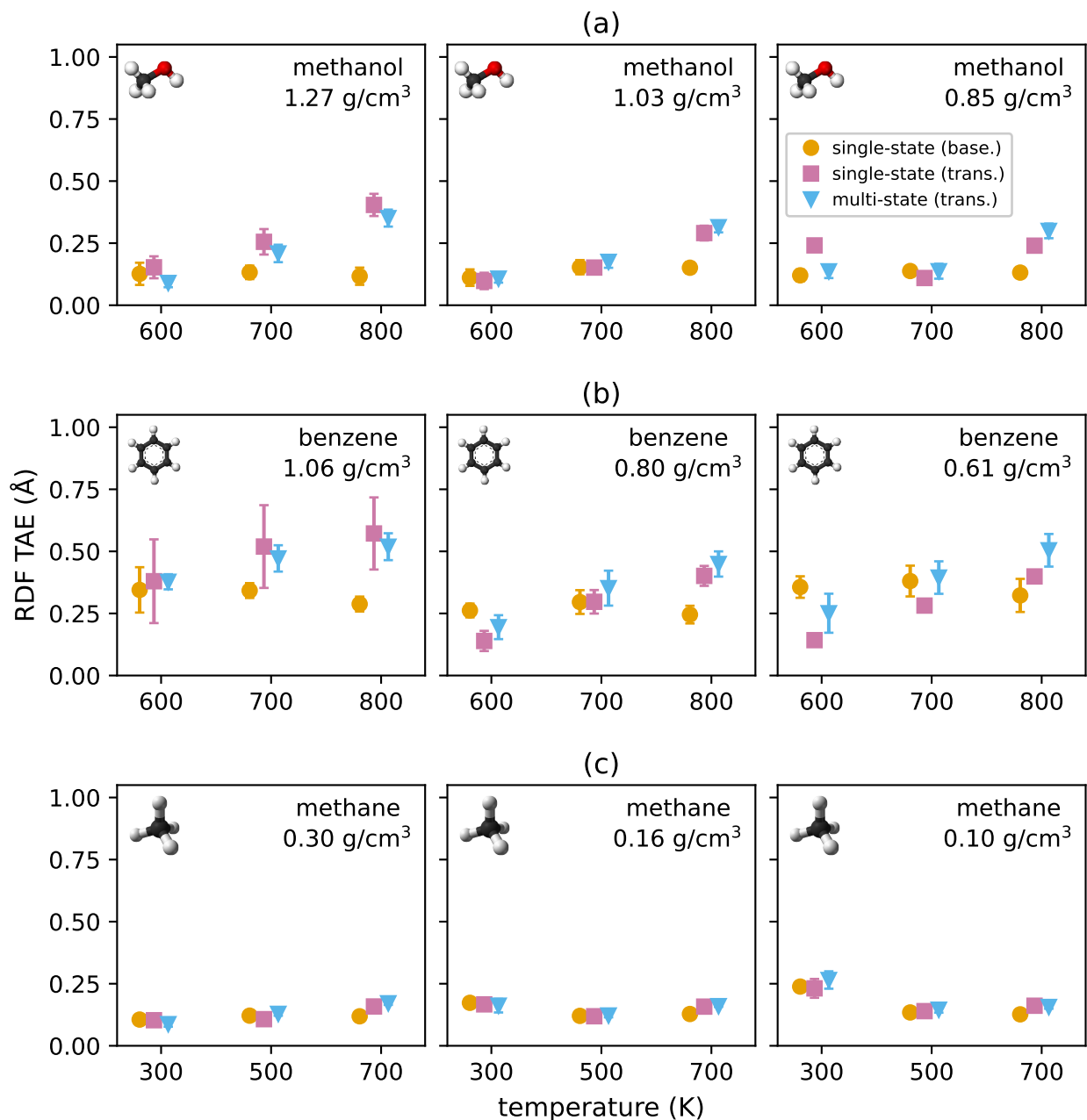


Figure 5: Total absolute error (TAE) between RDFs generated by AA MD and using various ML CG models for (a) methanol, (b) benzene, and (c) methane. The horizontal placement of the markers has been offset slightly for visual clarity. The error bars show the standard deviation calculated by constructing five ML CG models randomly sampled as described in the text.

For methane (Figure 5(c)), the single-state models perform best at the lowest temperature and highest density studied. This is an interesting observation because at this state point we expect the RDF to have the most structure and stronger correlations at larger r values in comparison to, for example, higher temperatures and lower densities. For the high density state points, the ML CG model for methane performs worse as the temperature is increased. Overall, the results in Figure 4 and Figure 5 illustrate that the ML CG methodology developed in this article can be applied to construct CG free energy functions that generate RDFs in strong agreement with AA results.

For the transferability test of the single-state models, the results show a surprising level of transferability for ML CG models; in general the TAEs for this test are almost always within a factor of 2 of the baseline single-state performance, with the exception of high-temperature, high-density methanol. Even more surprising, for several state points the single-state transferability performance is actually superior to the baseline models. Another observation is that significant variance between runs is observable for high-density benzene. Under more careful examination, these models produced slightly under-structured RDFs, and the variance between models is explained by the degree of under-structuring. A similar but less pronounced effect is visible for high-density methanol, where some variance appears for the single-state transferability model. In this case, the RDFs were not definitively under- or over-structured. Despite these fluctuations, the RDF quality is still reasonable.

Like the single-state transferability tests, the multi-state models exhibit remarkable transferability, in some instances even performing better than the single-state models. The higher variance observed in the single-state transferability tests for benzene has been significantly reduced. More detailed investigation of the underlying RDFs demonstrates that the multi-state ML CG models reproduce the AA statistics even through relatively large changes in the structural ordering of the fluid. Fig. 6 shows the most extreme state points (high-density, low-temperature and low-density, high-temperature) with respect to structural ordering. All of the molecules undergo significant changes in structural ordering across the space of ther-

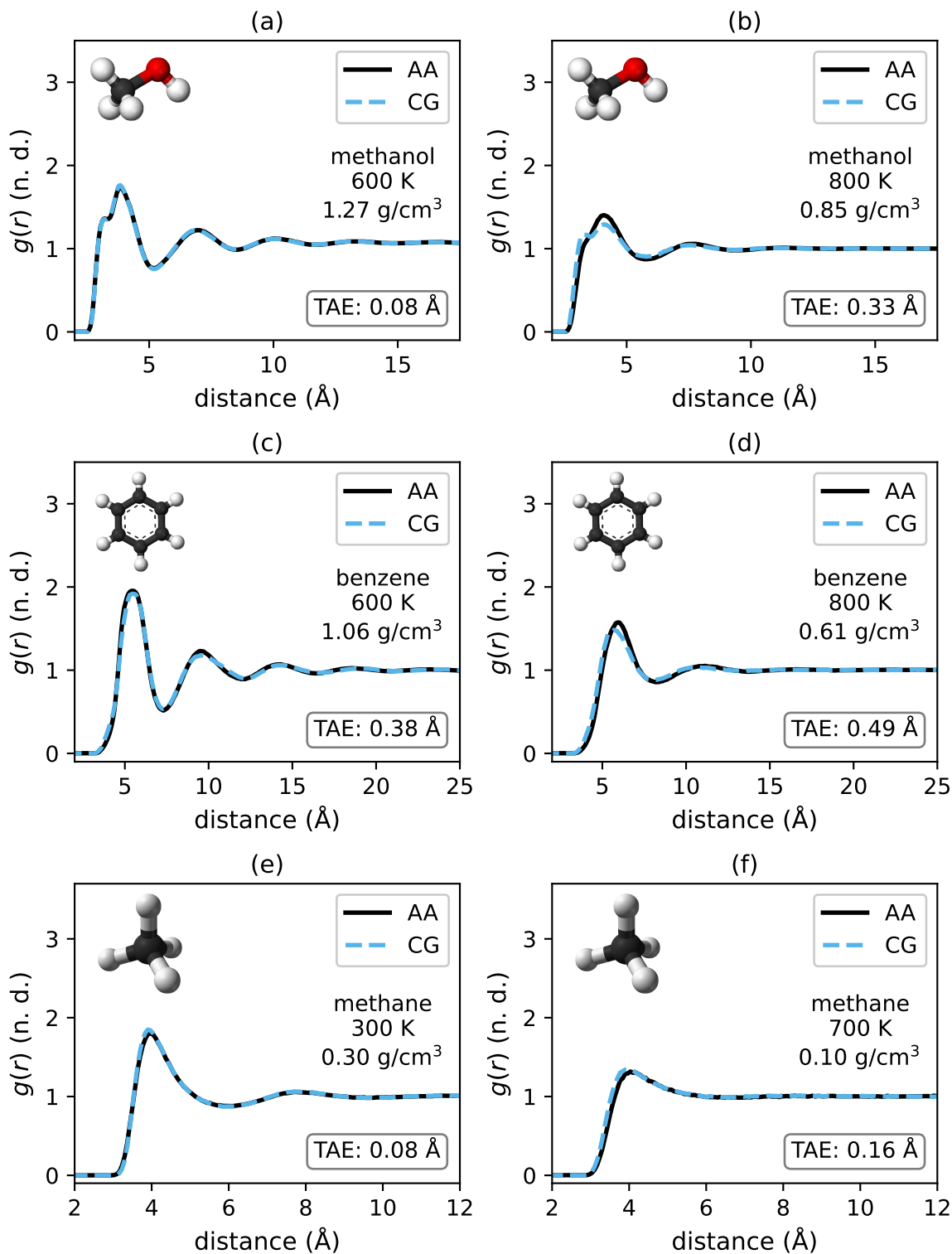


Figure 6: Comparison of reference RDFs generated by AA MD against RDFs generated via the ML CG multi-state model for (a) and (b) methanol, (c) and (d) benzene, and (e) and (f) methane. The state points represented are the left-most and right-most pictured in Figure 5 for each molecule, which have, respectively, the most and least structured RDFs.

modynamic states. We also tested whether the multi-state model can be productively applied to state points not present in the training data. We examined this for methanol by generating AA ground truth at two intermediate densities and two intermediate temperatures, yielding four new state points. The results of the multi-state model at these previously unseen points are shown in SI Figure S3, and demonstrate that the performance of the model does not significantly change when it is applied to intermediate state points not seen during training.

The ML CG workflow produces accurate models for a range of molecules and state points without tuning. The main parameter that might be adjusted is the interaction radius of the HIP-NN-TS architecture, but in this work, a uniform interaction distance of 12 Å was used for all molecules.

Computational cost

Computation times for ML CG training and MD are affordable enough to enable high-throughput analysis. For benzene and methane, training the ML CG models and running MD with the trained model each consistently took less than 30 minutes with a single NVIDIA A100 GPU. For methanol, each took consistently under one hour with the same architecture. As a result, in the course of this work, we were able to train more than 150 models and run more than 400 MD simulations. Scientifically, the most important aspect of automating these simulations was the addition of the repulsive potential determined as a pre-training step.

We also performed a comparison of our ML CG models to the AA HIP-NN-TS models of Ref. 49 using a periodic box of 1,024 methanol molecules. The AA ML potential could compute the forces approximately 0.3s on average, where the CG potential could compute the forces in approximately 0.04s on average. There is also a factor of four between the typical timestep for AA MD with an ML potential (0.25 fs) and the timestep used here (1 fs), leading to an overall 30 times faster simulation capacity with the ML CG method. Of course, there are many factors which will affect this number, such as variations in the

timesteps used, variations in the network architecture hyperparameters, the overall number of particles considered (1024 particles in the CG simulation does not typically saturate the GPU) and perhaps most importantly, variations in the number of atoms which are coarse-grained over. In regards to this last factor, methanol has a 6-to-1 ratio between atomistic and CG representations, but benzene has a 12-to-1 particle ratio between atomistic and CG representations, and furthermore has fewer neighbors in the same interaction radius, leading to reduced cost for message-passing operations in the neural network.

Conclusions

In this work, we built an ML CG workflow based on the bottom-up approach of Multi-Scale Coarse-Graining, for the first time using the Hierarchically Interacting Particle Neural Network (HIP-NN)^{48,49} with the aim of studying the transferability of coarse-grained models through varying thermodynamic conditions. In order to produce a robust workflow suitable for studying many molecules and state points, it was important to include a pairwise-repulsive potential, with parameters set before training. Otherwise, the workflow is very similar to training an AA potential using (fluctuating) forces, but not energies. As a result we were able to build more than 150 models and run over 400 MD simulations with those models, exploring the accuracy of models trained and used at the same state point, models trained and used at different state points, and models trained and used at multiple state points.

Our results show that the ML CG models here produce more consistent structural accuracy (as quantified by the RDF) than OpenMSCG pairwise CG models built using the same data, using liquid methanol at a variety of temperatures. Furthermore, training a model at 300K and deploying it across the range of 200K to 400K showed that the ML CG model is also significantly more transferable than the pairwise model. This is intriguing because although the neural network is highly expressive, it is not obvious how it distills many-body contributions to the CG free energy that make the potential more transferable. This is even

more surprising when considering the inherent noise in force-matching, which drastically reduces the model’s ability to match its training data precisely. This stands in contrast to the construction of AA potentials, where forces and energies can be matched during training to extreme precision.

We furthermore applied the ML CG workflow to study supercritical methanol, benzene, and methane across a range of densities and temperatures to study transferability from a more broad perspective. These conditions span significant variation in structural ordering in the fluids. We found that while overall model accuracy is superior using single-state models, models transferred across thermodynamic states do not produce extreme levels of error, and in some instances appear to paradoxically produce somewhat lower error than single-state models. We also tested building force-matched models trained across multiple state points. Although such a workflow violates the thermodynamic assumptions of coarse-graining (as the CG free energy is a function of temperature and density), there was no difficulty in producing these multi-state models, and they performed very well. However, given the relatively surprising level of transferability of single-state ML CG models, the comparative advantage of training to multiple state points was not strong. Multi-state training did improve on the variance of the RDF error for higher density methanol and benzene.

One area for future work is to explore transferability for cases of larger differences in structure, such as through phase transitions, e.g. between crystal and liquid. It might be that in this case, a multi-state training procedure shows stronger advantages. However, it is more difficult to automate the training data generation across thermodynamic phase changes, and this challenge would need to be addressed. Additionally, there are a wide variety of possible targets for coarse-graining, such as proteins, macromolecules, alloys, and liquid mixtures, which might be explored. Another future work possibility is to explore the potential for non-equilibrium coarse-grained simulations. Given the surprising transferability of these potentials, it may be possible to accurately model near-equilibrium conditions where temperatures and/or pressures evolve, either as a function of time or over space given

by some boundary conditions. An exciting possibility is to incorporate additional thermodynamics into the free energy function, essentially applying the concept of thermodynamically consistent learning⁴⁰ to coarse-graining; such a concept has recently been introduced and explored for the coarse-graining of hexane.⁷¹ With a wide range of recent improvements and ideas, machine learning based coarse-graining is poised to enable accurate simulations on large length and time scales across a wider range of thermodynamic conditions.

Data Availability Statement

The data that support the findings of this study are available from the corresponding authors upon reasonable request and institutional approval.

Acknowledgement

We acknowledge support from the Los Alamos National Laboratory (LANL) Directed Research and Development funds (LDRD). This research was performed in part at the Center for Nonlinear Studies (CNLS) at LANL. This research used resources provided by the Darwin testbed at LANL which is funded by the Computational Systems and Software Environments subprogram of LANL's Advanced Simulation and Computing program. LANL is operated by the Triad National Security, LLC, for the National Nuclear Security Administration of the U.S. Department of Energy (contract no. 89233218NCA000001).

We would like to thank David Rosenberger and Kipton Barros for helpful discussions.

Supporting Information Available

Further details on repulsive potential parameter selection, model training statistics, a discussion on training set size, and results of an interpolation test.

References

- (1) Izvekov, S.; Voth, G. A. Multiscale coarse graining of liquid-state systems. *J. Chem. Phys.* **2005**, *123*, 134105.
- (2) Lu, C.; Wu, C.; Ghoreishi, D.; Chen, W.; Wang, L.; Damm, W.; Ross, G. A.; Dahlgren, M. K.; Russell, E.; Von Bargen, C. D.; Abel, R.; Friesner, R. A.; Harder, E. D. OPLS4: Improving Force Field Accuracy on Challenging Regimes of Chemical Space. *J. Chem. Theory Comput.* **2021**, *17*, 4291–4300.
- (3) Unke, O. T.; Chmiela, S.; Sauceda, H. E.; Gastegger, M.; Poltavsky, I.; Schütt, K. T.; Tkatchenko, A.; Müller, K.-R. Machine Learning Force Fields. *Chem. Rev.* **2021**, *121*, 10142–10186.
- (4) Polêto, M. D.; Lemkul, J. A. Integration of experimental data and use of automated fitting methods in developing protein force fields. *Comm. Chem.* **2022**, *5*, 38.
- (5) Zongo, K.; Béland, L.; Ouellet-Plamondon, C. First-principles database for fitting a machine-learning silicon interatomic force field. *MRS Advances* **2022**, *7*, 39–47.
- (6) Matin, S.; Allen, A. E. A.; Smith, J.; Lubbers, N.; Jadrich, R. B.; Messerly, R.; Nebgen, B.; Li, Y. W.; Tretiak, S.; Barros, K. Machine Learning Potentials with the Iterative Boltzmann Inversion: Training to Experiment. *J. Chem. Theory Comput.* **2024**, *20*, 1274–1281.
- (7) Botu, V.; Batra, R.; Chapman, J.; Ramprasad, R. Machine Learning Force Fields: Construction, Validation, and Outlook. *J. Phys. Chem. C* **2017**, *121*, 511–522.
- (8) Wu, S.; Yang, X.; Zhao, X.; Li, Z.; Lu, M.; Xie, X.; Yan, J. Applications and Advances in Machine Learning Force Fields. *J. Chem. Inf. Model.* **2023**, *63*, 6972–6985.
- (9) Rosenberger, D.; Smith, J. S.; Garcia, A. E. Modeling of Peptides with Classical and

- Novel Machine Learning Force Fields: A Comparison. *J. Phys. Chem. B* **2021**, *125*, 3598–3612.
- (10) Frenkel, D.; Smit, B. *Understanding molecular simulation: From algorithms to application*; Academic Press: NY, 1996.
- (11) Fedik, N.; Zubatyuk, R.; Kulichenko, M.; Lubbers, N.; Smith, J. S.; Nebgen, B.; Messerly, R.; Li, Y. W.; Boldyrev, A. I.; Barros, K.; others Extending machine learning beyond interatomic potentials for predicting molecular properties. *Nat. Rev. Chem.* **2022**, *6*, 653–672.
- (12) Shih, A. Y.; Arkhipov, A.; Freddolino, P. L.; ; Schulten, K. Coarse Grained Protein-Lipid Model with Application to Lipoprotein Particles. *J. Phys. Chem. B* **2006**, *110*, 3674–3684.
- (13) Saunders, M. G.; Voth, G. A. Coarse-Graining Methods for Computational Biology. *Annu. Rev. Biophys.* **2013**, *42*, 73–93.
- (14) Lu, L.; Dama, J. F.; Voth, G. A. Fitting coarse-grained distribution functions through an iterative force-matching method. *J. Chem. Phys.* **2013**, *139*, 121906.
- (15) Noid, W. G. Perspective: Coarse-grained models for biomolecular systems. *J. Chem. Phys.* **2013**, *139*, 090901.
- (16) Jin, J.; Pak, A. J.; Durumeric, A. E.; Loose, T. D.; Voth, G. A. Bottom-up coarse-graining: Principles and perspectives. *J. Chem. Theory Comput.* **2022**, *18*, 5759–5791.
- (17) Dama, J. F.; Sinititskiy, A. V.; McCullagh, M.; Weare, J.; Roux, B.; Dinner, A. R.; Voth, G. A. The Theory of Ultra-Coarse-Graining. 1. General Principles. *J. Chem. Theory Comput.* **2013**, *9*, 2466–2480.

- (18) Davtyan, A.; Dama, J. F.; Sinitskiy, A. V.; Voth, G. A. The Theory of Ultra-Coarse-Graining. 2. Numerical Implementation. *J. Chem. Theory Comput.* **2014**, *10*, 5265–5275.
- (19) Brennan, J. K.; Lísal, M.; Moore, J. D.; Izvekov, S.; Schweigert, I. V.; Larentzos, J. P. Coarse-Grain Model Simulations of Nonequilibrium Dynamics in Heterogeneous Materials. *J. Phys. Chem. Lett.* **2014**, *5*, 2144–2149.
- (20) Schilling, T. Coarse-grained modelling out of equilibrium. *Phys. Rep.* **2022**, *972*, 1–45.
- (21) Marrink, S. J.; Risselada, H. J.; Yefimov, S.; Tieleman, D. P.; de Vries, A. H. The MARTINI Force Field: Coarse Grained Model for Biomolecular Simulations. *J. Phys. Chem. B* **2007**, *111*, 7812–7824, PMID: 17569554.
- (22) Noid, W. G. Perspective: Advances, Challenges, and Insight for Predictive Coarse-Grained Models. *J. Phys. Chem. B* **2023**, *127*, 4174–4207.
- (23) Palma Banos, M.; Popov, A. V.; Hernandez, R. Representability and Dynamical Consistency in Coarse-Grained Models. *J. Phys. Chem. B* **2024**, *128*, 1506–1514.
- (24) Craven, G. T.; Popov, A. V.; Hernandez, R. Structure of a tractable stochastic mimic of soft particles. *Soft Matter* **2014**, *10*, 5350–5361.
- (25) Moore, T. C.; Iacovella, C. R.; McCabe, C. Derivation of coarse-grained potentials via multistate iterative Boltzmann inversion. *J. Chem. Phys.* **2014**, *140*, 224104.
- (26) Dunn, N. J. H.; Noid, W. G. Bottom-up coarse-grained models that accurately describe the structure, pressure, and compressibility of molecular liquids. *J. Chem. Phys.* **2015**, *143*, 243148.
- (27) Moradzadeh, A.; Aluru, N. R. Transfer-Learning-Based Coarse-Graining Method for Simple Fluids: Toward Deep Inverse Liquid-State Theory. *J. Phys. Chem. Lett.* **2019**, *10*, 1242–1250.

- (28) Narros, A.; Moreno, A. J.; Likos, C. N. Influence of topology on effective potentials: coarse-graining ring polymers. *Soft Matter* **2010**, *6*, 2435–2441.
- (29) Craven, G. T.; Popov, A. V.; Hernandez, R. Effective Surface Coverage of Coarse-Grained Soft Matter. *J. Phys. Chem. B* **2014**, *118*, 14092–14102.
- (30) Zhang, P.; Wang, Q. Solvent entropy and coarse-graining of polymer lattice models. *Soft Matter* **2013**, *9*, 11183–11187.
- (31) Ricci, E.; Vergadou, N. Integrating Machine Learning in the Coarse-Grained Molecular Simulation of Polymers. *J. Phys. Chem. B* **2023**, *127*, 2302–2322.
- (32) Chennakesavalu, S.; Toomer, D. J.; Rotskoff, G. M. Ensuring thermodynamic consistency with invertible coarse-graining. *J. Chem. Phys.* **2023**, *158*, 124126.
- (33) Dunn, N. J. H.; Foley, T. T.; Noid, W. G. Van der Waals Perspective on Coarse-Graining: Progress toward Solving Representability and Transferability Problems. *Acc. Chem. Res.* **2016**, *49*, 2832–2840.
- (34) Rosenberger, D.; van der Vegt, N. F. A. Addressing the temperature transferability of structure based coarse graining models. *Phys. Chem. Chem. Phys.* **2018**, *20*, 6617–6628.
- (35) Mullinax, J. W.; Noid, W. G. Extended ensemble approach for deriving transferable coarse-grained potentials. *J. Chem. Phys.* **2009**, *131*, 104110.
- (36) Shen, K.; Sherck, N.; Nguyen, M.; Yoo, B.; Köhler, S.; Speros, J.; Delaney, K. T.; Fredrickson, G. H.; Shell, M. S. Learning composition-transferable coarse-grained models: Designing external potential ensembles to maximize thermodynamic information. *J. Chem. Phys.* **2020**, *153*, 154116.
- (37) Guenza, M. G.; Dinpajoo, M.; McCarty, J.; Lyubimov, I. Y. Accuracy, Transferability, and Efficiency of Coarse-Grained Models of Molecular Liquids. *J. Phys. Chem. B* **2018**, *122*, 10257–10278.

- (38) Craven, G. T.; Lubbers, N.; Barros, K.; Tretiak, S. Machine learning approaches for structural and thermodynamic properties of a Lennard-Jones fluid. *J. Chem. Phys.* **2020**, *153*, 104502.
- (39) Craven, G. T.; Lubbers, N.; Barros, K.; Tretiak, S. *Ex Machina* Determination of Structural Correlation Functions. *J. Phys. Chem. Lett.* **2020**, *11*, 4372–4378.
- (40) Rosenberger, D.; Barros, K.; Germann, T. C.; Lubbers, N. Machine learning of consistent thermodynamic models using automatic differentiation. *Phys. Rev. E* **2022**, *105*, 045301.
- (41) Harrison, J. A.; Schall, J. D.; Maskey, S.; Mikulski, P. T.; Knippenberg, M. T.; Morrow, B. H. Review of force fields and intermolecular potentials used in atomistic computational materials research. *Applied Physics Reviews* **2018**, *5*, 031104.
- (42) Kulichenko, M.; Smith, J. S.; Nebgen, B.; Li, Y. W.; Fedik, N.; Boldyrev, A. I.; Lubbers, N.; Barros, K.; Tretiak, S. The Rise of Neural Networks for Materials and Chemical Dynamics. *The Journal of Physical Chemistry Letters* **2021**, *12*, 6227–6243, PMID: 34196559.
- (43) Smith, J. S.; Isayev, O.; Roitberg, A. E. ANI-1: an extensible neural network potential with DFT accuracy at force field computational cost. *Chem. Sci.* **2017**, *8*, 3192–3203.
- (44) Thaler, S.; Stupp, M.; Zavadlav, J. Deep coarse-grained potentials via relative entropy minimization. *J. Chem. Phys.* **2022**, *157*, 244103.
- (45) Wang, J.; Olsson, S.; Wehmeyer, C.; Pérez, A.; Charron, N. E.; De Fabritiis, G.; Noé, F.; Clementi, C. Machine learning of coarse-grained molecular dynamics force fields. *ACS Central Science* **2019**, *5*, 755–767.
- (46) Fu, X.; Xie, T.; Rebello, N. J.; Olsen, B. D.; Jaakkola, T. Simulate time-integrated

- coarse-grained molecular dynamics with geometric machine learning. *arXiv preprint arXiv:2204.10348* **2022**,
- (47) Noid, W. G.; Chu, J.-W.; Ayton, G. S.; Krishna, V.; Izvekov, S.; Voth, G. A.; Das, A.; Andersen, H. C. The multiscale coarse-graining method. I. A rigorous bridge between atomistic and coarse-grained models. *J. Chem. Phys.* **2008**, *128*.
- (48) Lubbers, N.; Smith, J. S.; Barros, K. Hierarchical modeling of molecular energies using a deep neural network. *J. Chem. Phys.* **2018**, *148*, 241715.
- (49) Chigaev, M.; Smith, J. S.; Anaya, S.; Nebgen, B.; Bettencourt, M.; Barros, K.; Lubbers, N. Lightweight and effective tensor sensitivity for atomistic neural networks. *J. Chem. Phys.* **2023**, *158*, 184108.
- (50) Peng, Y.; Pak, A. J.; Durumeric, A. E.; Sahrman, P. G.; Mani, S.; Jin, J.; Loose, T. D.; Beiter, J.; Voth, G. A. OpenMSCG: A Software Tool for Bottom-Up Coarse-Graining. *J. Phys. Chem. B* **2023**, *127*, 8537–8550.
- (51) Noid, W.; Chu, J.-W.; Ayton, G. S.; Voth, G. A. Multiscale coarse-graining and structural correlations: Connections to liquid-state theory. *J. Phys. Chem. B* **2007**, *111*, 4116–4127.
- (52) Ciccotti, G.; Kapral, R.; Vanden-Eijnden, E. Blue Moon Sampling, Vectorial Reaction Coordinates, and Unbiased Constrained Dynamics. *ChemPhysChem* **2005**, *6*, 1809–1814.
- (53) Smith, J. S.; Lubbers, N.; Thompson, A. P.; Barros, K. Simple and efficient algorithms for training machine learning potentials to force data. *arXiv preprint arXiv:2006.05475* **2020**,
- (54) MSCG Tutorials: Lesson 01. Force-Matching Single-Site Methanol. <https://>

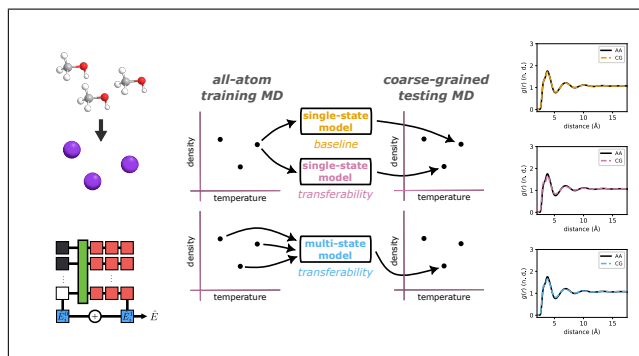
software.rcc.uchicago.edu/mscg/tutorials/lesson-01/README.html, Accessed: 2024-03-04.

- (55) Lindahl, E.; Hess, B.; Van Der Spoel, D. GROMACS 3.0: a package for molecular simulation and trajectory analysis. *Molecular modeling annual* **2001**, *7*, 306–317.
- (56) Jorgensen, W. L.; Maxwell, D. S.; Tirado-Rives, J. Development and Testing of the OPLS All-Atom Force Field on Conformational Energetics and Properties of Organic Liquids. *J. Am. Chem. Soc.* **1996**, *118*, 11225–11236.
- (57) Thompson, A. P.; Aktulga, H. M.; Berger, R.; Bolintineanu, D. S.; Brown, W. M.; Crozier, P. S.; in 't Veld, P. J.; Kohlmeyer, A.; Moore, S. G.; Nguyen, T. D.; Shan, R.; Stevens, M. J.; Tranchida, J.; Trott, C.; Plimpton, S. J. LAMMPS - a flexible simulation tool for particle-based materials modeling at the atomic, meso, and continuum scales. *Comp. Phys. Comm.* **2022**, *271*, 108171.
- (58) Schmid, N.; Eichenberger, A. P.; Choutko, A.; Riniker, S.; Winger, M.; Mark, A. E.; van Gunsteren, W. F. Definition and testing of the GROMOS force-field versions 54A7 and 54B7. *European Biophysics Journal* **2011**, 843–856.
- (59) Malde, A. K.; Zuo, L.; Breeze, M.; Stroet, M.; Poger, D.; Nair, P. C.; Oostenbrink, C.; Mark, A. E. An Automated Force Field Topology Builder (ATB) and Repository: Version 1.0. *J. Chem. Theory Comput.* **2011**, *7*, 4026–4037.
- (60) Stroet, M.; Caron, B.; Visscher, K. M.; Geerke, D. P.; Malde, A. K.; Mark, A. E. Automated Topology Builder Version 3.0: Prediction of Solvation Free Enthalpies in Water and Hexane. *J. Chem. Theory Comput.* **2018**, *14*, 5834–5845.
- (61) Martínez, L.; Andrade, R.; Birgin, E. G.; Martínez, J. M. PACKMOL: A package for building initial configurations for molecular dynamics simulations. *J. Comput. Chem.* **2009**, *30*, 2157–2164.

- (62) Jewett, A. I.; Stelter, D.; Lambert, J.; Saladi, S. M.; Roscioni, O. M.; Ricci, M.; Autin, L.; Maritan, M.; Bashusqeh, S. M.; Keyes, T.; Dame, R. T.; Shea, J.-E.; Jensen, G. J.; Goodsell, D. S. Moltemplate: A Tool for Coarse-Grained Modeling of Complex Biological Matter and Soft Condensed Matter Physics. *J. Mol. Biol.* **2021**, *433*, 166841, Computation Resources for Molecular Biology.
- (63) Rosenberger, D.; Lubbers, N.; Germann, T. C. Evaluating diffusion and the thermodynamic factor for binary ionic mixtures. *Physics of Plasmas* **2020**, *27*, 102705.
- (64) Trokhymchuk, A.; Nezbeda, I.; Jirsák, J.; Henderson, D. Hard-sphere radial distribution function again. *J. Chem. Phys.* **2005**, *123*, 024501.
- (65) Hansen, J. P.; McDonald, I. R. *Theory of simple liquids*; Academic press, 2006.
- (66) Gray, C. G.; Gubbins, K. E. *Theory of molecular fluids*; Clarendon Press Oxford, 1984; Vol. 1.
- (67) Foidl, C. Exact pair distribution function and structure factor for a one-dimensional hard rod mixture. *J. Chem. Phys.* **1986**, *85*, 410–417.
- (68) Krämer, A.; Durumeric, A. E. P.; Charron, N. E.; Chen, Y.; Clementi, C.; Noé, F. Statistically Optimal Force Aggregation for Coarse-Graining Molecular Dynamics. *The Journal of Physical Chemistry Letters* **2023**, *14*, 3970–3979, PMID: 37079800.
- (69) Izvekov, S.; Voth, G. A. A multiscale coarse-graining method for biomolecular systems. *J. Phys. Chem. B* **2005**, *109*, 2469–2473.
- (70) Noid, W.; Liu, P.; Wang, Y.; Chu, J.-W.; Ayton, G. S.; Izvekov, S.; Andersen, H. C.; Voth, G. A. The multiscale coarse-graining method. II. Numerical implementation for coarse-grained molecular models. *J. Chem. Phys.* **2008**, *128*.
- (71) Duschatko, B. R.; Fu, X.; Owen, C.; Xie, Y.; Musaelian, A.; Jaakkola, T.; Kozinsky, B.

Thermodynamically Informed Multimodal Learning of High-Dimensional Free Energy Models in Molecular Coarse Graining. 2024.

TOC Graphic



Supporting Information:

Thermodynamic Transferability in Coarse-Grained Force Fields using Graph Neural Networks

Emily Shinkle,^{*,†} Aleksandra Pachalieva,^{‡,¶} Riti Bahl,^{§,||} Sakib Matin,^{||} Brendan Gifford,^{||} Galen T. Craven,^{||} and Nicholas Lubbers^{*,†}

[†]*Computer, Computational, and Statistical Sciences Division, Los Alamos National Laboratory, Los Alamos, NM 87545, USA*

[‡]*Earth and Environmental Sciences Division, Los Alamos National Laboratory, Los Alamos, NM 87545, USA*

[¶]*Center for Nonlinear Studies, Los Alamos National Laboratory, Los Alamos, NM 87545, USA*

[§]*Department of Mathematics, Emory University, Atlanta, GA 30322*

^{||}*Theoretical Division, Los Alamos National Laboratory, Los Alamos, NM 87545, USA*

E-mail: eshinkle@lanl.gov; nlubbers@lanl.gov

Repulsive potential

To help the HIP-NN-TS models handle pairs of beads whose distance is less than that of any pairs in the set of training data, a repulsive pair potential is added. The potential is of the form

$$E_{\text{rep}}(r) = E_0 e^{-ar} \quad (1)$$

where r is the pair distance, $E_0, a > 0$ are parameters chosen for each network, and $E_{\text{rep}}(r)$ is the contribution to the energy potential from the pair. The following values are used to calculate E_0 and a :

Variable name	Variable interpretation	Value(s) used
t	pair distance at which repulsive potential should be minimal	lowest pair distance in training data (outliers excluded)
s	strength of force on particle due to repulsive potential at $t - d$	the mean force magnitude from the training data
d	see preceding row	0.15 (Angstroms)
p	percentage of s that remains at t	0.05

Based on these values, the values of a and E_0 are calculated as

$$a = \frac{1}{d} \ln \left(\frac{1}{p} \right) \text{ and } E_0 = \frac{pse^{at}}{a}. \quad (2)$$

Then the force on one particle from another particle at distance r due to the repulsive potential is

$$F_{\text{rep}}(r) = -\frac{\partial E_{\text{rep}}}{\partial dr}(r) = aE_0e^{-ar}, \quad (3)$$

and one can verify that $F_{\text{rep}}(t) = ps$ and $F_{\text{rep}}(t - d) = s$.

Training statistics

Here the statistics of the trained HIP-NN-TS models are reported. Recall that the Total Loss is the sum of Force MAE and Force RMSE. The Force R^2 is also reported. Each statistic is displayed as the mean plus or minus the standard deviation across the five variants of that model which were trained.

Methanol

Temp.	Density	Dataset	Force MAE	Force RMSE	Total Loss	Force R^2
600 K	1.27 g/cm ³	validation	8.982 ± 0.002	11.845 ± 0.002	20.826 ± 0.003	0.138 ± 0.000
		testing	9.010 ± 0.002	11.862 ± 0.002	20.872 ± 0.003	0.140 ± 0.000
		training	8.963 ± 0.005	11.819 ± 0.006	20.782 ± 0.012	0.143 ± 0.001
	1.03 g/cm ³	validation	6.560 ± 0.001	8.877 ± 0.002	15.436 ± 0.001	0.153 ± 0.000
		testing	6.545 ± 0.001	8.860 ± 0.001	15.405 ± 0.001	0.150 ± 0.000
		training	6.532 ± 0.003	8.834 ± 0.002	15.366 ± 0.004	0.155 ± 0.000
	0.85 g/cm ³	validation	5.246 ± 0.001	7.255 ± 0.002	12.501 ± 0.003	0.156 ± 0.001
		testing	5.246 ± 0.001	7.260 ± 0.003	12.506 ± 0.004	0.161 ± 0.001
		training	5.263 ± 0.003	7.288 ± 0.005	12.551 ± 0.007	0.161 ± 0.001
700 K	1.27 g/cm ³	validation	9.874 ± 0.001	13.096 ± 0.001	22.970 ± 0.002	0.138 ± 0.000
		testing	9.867 ± 0.001	13.084 ± 0.001	22.951 ± 0.003	0.135 ± 0.000
		training	9.872 ± 0.003	13.079 ± 0.003	22.950 ± 0.007	0.137 ± 0.000
	1.03 g/cm ³	validation	7.146 ± 0.002	9.742 ± 0.001	16.888 ± 0.001	0.147 ± 0.000
		testing	7.138 ± 0.003	9.769 ± 0.001	16.907 ± 0.002	0.146 ± 0.000
		training	7.131 ± 0.004	9.741 ± 0.002	16.872 ± 0.006	0.149 ± 0.000
	0.85 g/cm ³	validation	5.615 ± 0.001	7.872 ± 0.001	13.487 ± 0.002	0.152 ± 0.000
		testing	5.640 ± 0.001	7.912 ± 0.001	13.552 ± 0.001	0.150 ± 0.000
		training	5.624 ± 0.001	7.906 ± 0.001	13.529 ± 0.001	0.151 ± 0.000

Methanol continued

Temp.	Density	Dataset	Force MAE	Force RMSE	Total Loss	Force R^2
800 K	1.27 g/cm ³	validation	10.803 \pm 0.002	14.375 \pm 0.003	25.178 \pm 0.004	0.132 \pm 0.000
		testing	10.704 \pm 0.001	14.272 \pm 0.001	24.976 \pm 0.001	0.136 \pm 0.000
		training	10.762 \pm 0.004	14.330 \pm 0.006	25.092 \pm 0.011	0.137 \pm 0.001
	1.03 g/cm ³	validation	7.686 \pm 0.002	10.557 \pm 0.002	18.243 \pm 0.005	0.146 \pm 0.000
		testing	7.678 \pm 0.002	10.574 \pm 0.002	18.253 \pm 0.003	0.145 \pm 0.000
		training	7.682 \pm 0.003	10.580 \pm 0.003	18.261 \pm 0.006	0.148 \pm 0.001
	0.85 g/cm ³	validation	5.985 \pm 0.002	8.512 \pm 0.002	14.498 \pm 0.002	0.149 \pm 0.000
		testing	5.979 \pm 0.003	8.481 \pm 0.002	14.461 \pm 0.001	0.148 \pm 0.000
		training	5.979 \pm 0.002	8.499 \pm 0.004	14.478 \pm 0.003	0.151 \pm 0.001
Multi-state		validation	7.370 \pm 0.001	10.252 \pm 0.002	17.622 \pm 0.001	0.142 \pm 0.000
		testing	7.849 \pm 0.001	10.910 \pm 0.003	18.760 \pm 0.004	0.143 \pm 0.000
		training	7.539 \pm 0.003	10.485 \pm 0.003	18.024 \pm 0.006	0.141 \pm 0.001

Benzene

Temp.	Density	Dataset	Force MAE	Force RMSE	Total Loss	Force R^2
600 K	1.06 g/cm ³	validation	6.710 ± 0.003	9.084 ± 0.003	15.794 ± 0.006	0.161 ± 0.001
		testing	6.726 ± 0.003	9.092 ± 0.004	15.818 ± 0.006	0.160 ± 0.001
		training	6.701 ± 0.004	9.058 ± 0.004	15.759 ± 0.007	0.162 ± 0.001
	0.80 g/cm ³	validation	3.990 ± 0.002	5.833 ± 0.002	9.824 ± 0.002	0.149 ± 0.001
		testing	4.030 ± 0.002	5.900 ± 0.002	9.929 ± 0.002	0.146 ± 0.001
		training	4.014 ± 0.002	5.879 ± 0.002	9.892 ± 0.003	0.147 ± 0.001
	0.61 g/cm ³	validation	2.843 ± 0.002	4.491 ± 0.002	7.334 ± 0.001	0.127 ± 0.001
		testing	2.844 ± 0.002	4.481 ± 0.002	7.325 ± 0.001	0.129 ± 0.001
		training	2.868 ± 0.006	8.019 ± 1.734	10.886 ± 1.740	-1.865 ± 1.038
700 K	1.06 g/cm ³	validation	7.555 ± 0.002	10.257 ± 0.002	17.812 ± 0.003	0.159 ± 0.000
		testing	7.558 ± 0.002	10.284 ± 0.002	17.842 ± 0.003	0.161 ± 0.000
		training	7.562 ± 0.002	10.275 ± 0.002	17.837 ± 0.003	0.163 ± 0.000
	0.80 g/cm ³	validation	4.482 ± 0.002	6.612 ± 0.001	11.094 ± 0.002	0.147 ± 0.000
		testing	4.504 ± 0.002	6.647 ± 0.002	11.151 ± 0.002	0.146 ± 0.000
		training	4.495 ± 0.002	6.636 ± 0.002	11.131 ± 0.003	0.147 ± 0.001
	0.61 g/cm ³	validation	3.168 ± 0.003	5.061 ± 0.003	8.229 ± 0.002	0.133 ± 0.001
		testing	3.144 ± 0.004	5.016 ± 0.003	8.161 ± 0.002	0.131 ± 0.001
		training	3.173 ± 0.003	6.907 ± 0.342	10.080 ± 0.344	-0.621 ± 0.159
800 K	1.06 g/cm ³	validation	8.410 ± 0.002	11.480 ± 0.003	19.890 ± 0.001	0.161 ± 0.000
		testing	8.383 ± 0.001	11.409 ± 0.003	19.791 ± 0.002	0.162 ± 0.000
		training	8.416 ± 0.002	11.477 ± 0.005	19.892 ± 0.006	0.163 ± 0.001
	0.80 g/cm ³	validation	4.988 ± 0.003	7.382 ± 0.002	12.369 ± 0.001	0.150 ± 0.000
		testing	4.991 ± 0.002	7.370 ± 0.003	12.361 ± 0.001	0.152 ± 0.001
		training	4.998 ± 0.002	7.405 ± 0.002	12.403 ± 0.002	0.151 ± 0.000
	0.61 g/cm ³	validation	3.518 ± 0.011	5.699 ± 0.015	9.217 ± 0.017	0.129 ± 0.005
		testing	3.502 ± 0.011	5.631 ± 0.007	9.133 ± 0.011	0.137 ± 0.002
		training	3.504 ± 0.011	5.659 ± 0.007	9.164 ± 0.014	0.134 ± 0.002

Benzene continued

			Force MAE	Force RMSE	Total Loss	Force R^2
Temp.	Density	Dataset				
Multi-state		validation	4.862 ± 0.003	7.381 ± 0.007	12.243 ± 0.008	0.145 ± 0.002
		testing	5.464 ± 0.009	8.519 ± 0.534	13.983 ± 0.543	0.081 ± 0.120
		training	5.078 ± 0.006	7.775 ± 0.181	12.852 ± 0.187	0.125 ± 0.041

Methane

Temp.	Density	Dataset	Force MAE	Force RMSE	Total Loss	Force R^2
300 K	0.30 g/cm ³	validation	0.771 ± 0.001	1.410 ± 0.001	2.180 ± 0.000	0.528 ± 0.001
		testing	0.765 ± 0.001	1.388 ± 0.001	2.153 ± 0.000	0.534 ± 0.001
		training	0.765 ± 0.001	1.390 ± 0.001	2.156 ± 0.000	0.533 ± 0.001
	0.16 g/cm ³	validation	0.429 ± 0.001	0.978 ± 0.001	1.408 ± 0.000	0.535 ± 0.001
		testing	0.429 ± 0.001	0.970 ± 0.001	1.399 ± 0.000	0.541 ± 0.001
		training	0.432 ± 0.001	0.986 ± 0.001	1.418 ± 0.000	0.538 ± 0.001
	0.10 g/cm ³	validation	0.285 ± 0.000	0.772 ± 0.000	1.056 ± 0.000	0.551 ± 0.000
		testing	0.289 ± 0.000	0.807 ± 0.001	1.097 ± 0.000	0.535 ± 0.001
		training	0.283 ± 0.000	0.780 ± 0.001	1.063 ± 0.000	0.545 ± 0.001
500 K	0.30 g/cm ³	validation	1.107 ± 0.002	2.092 ± 0.001	3.199 ± 0.001	0.520 ± 0.001
		testing	1.098 ± 0.001	2.096 ± 0.001	3.194 ± 0.001	0.527 ± 0.000
		training	1.095 ± 0.002	2.080 ± 0.001	3.175 ± 0.001	0.527 ± 0.000
	0.16 g/cm ³	validation	0.568 ± 0.002	1.347 ± 0.002	1.914 ± 0.000	0.538 ± 0.001
		testing	0.570 ± 0.002	1.397 ± 0.002	1.967 ± 0.001	0.516 ± 0.001
		training	0.566 ± 0.002	1.377 ± 0.002	1.943 ± 0.001	0.527 ± 0.001
	0.10 g/cm ³	validation	0.356 ± 0.001	1.070 ± 0.001	1.426 ± 0.000	0.522 ± 0.001
		testing	0.350 ± 0.001	1.051 ± 0.001	1.400 ± 0.001	0.529 ± 0.001
		training	0.348 ± 0.001	1.037 ± 0.001	1.385 ± 0.001	0.532 ± 0.001
700 K	0.30 g/cm ³	validation	1.439 ± 0.002	2.827 ± 0.002	4.266 ± 0.001	0.516 ± 0.001
		testing	1.458 ± 0.001	2.873 ± 0.002	4.332 ± 0.001	0.511 ± 0.001
		training	1.439 ± 0.002	2.815 ± 0.002	4.254 ± 0.001	0.521 ± 0.001
	0.16 g/cm ³	validation	0.714 ± 0.001	1.826 ± 0.001	2.540 ± 0.001	0.520 ± 0.001
		testing	0.705 ± 0.001	1.808 ± 0.001	2.513 ± 0.000	0.522 ± 0.000
		training	0.718 ± 0.001	1.830 ± 0.001	2.548 ± 0.001	0.519 ± 0.001
	0.10 g/cm ³	validation	0.427 ± 0.001	1.362 ± 0.001	1.789 ± 0.000	0.520 ± 0.001
		testing	0.429 ± 0.001	1.356 ± 0.001	1.785 ± 0.000	0.519 ± 0.001
		training	0.429 ± 0.001	1.360 ± 0.001	1.790 ± 0.001	0.527 ± 0.001

Methane continued

			Force MAE	Force RMSE	Total Loss	Force R^2
Temp.	Density	Dataset				
Multi-state		validation	0.632 ± 0.001	1.539 ± 0.001	2.172 ± 0.001	0.523 ± 0.001
		testing	0.761 ± 0.001	1.832 ± 0.002	2.593 ± 0.001	0.500 ± 0.001
		training	0.681 ± 0.001	1.655 ± 0.001	2.337 ± 0.001	0.515 ± 0.001

Below are the statistics for the models trained for the comparison with the OpenMSCG method.

Methanol

Temp.	Dataset	Force MAE	Force RMSE	Force R^2	Total Loss
200 K	training	2.5441	3.3669	0.2763	5.9110
	validation	2.5507	3.3764	0.2736	5.9271
	testing	2.4940	3.3089	0.3042	5.8029
220 K	training	2.6335	3.4968	0.2720	6.1302
	validation	2.6375	3.5062	0.2708	6.1437
	testing	2.6449	3.5087	0.2614	6.1536
240 K	training	2.7362	3.6470	0.2695	6.3832
	validation	2.7248	3.6257	0.2712	6.3505
	testing	2.7404	3.6462	0.2455	6.3866
260 K	training	2.8349	3.7875	0.2614	6.6224
	validation	2.8323	3.7857	0.2623	6.6181
	testing	2.7616	3.6527	0.2906	6.4143
280 K	training	2.9456	3.9430	0.2529	6.8886
	validation	2.9440	3.9416	0.2530	6.8855
	testing	2.8975	3.9620	0.2844	6.8595
300 K	training	3.0370	4.0829	0.2438	7.1199
	validation	3.0356	4.0772	0.2474	7.1128
	testing	2.9605	3.9363	0.2622	6.8968
320 K	training	3.1356	4.2195	0.2367	7.3551
	validation	3.1319	4.2098	0.2355	7.3417
	testing	3.0640	4.0750	0.2544	7.1390
340 K	training	3.2318	4.3665	0.2278	7.5983
	validation	3.2320	4.3685	0.2240	7.6005
	testing	3.2447	4.3918	0.2164	7.6365

Methanol continued

		Force MAE	Force RMSE	Force R^2	Total Loss
Temp.	Dataset				
360 K	training	3.3178	4.4953	0.2221	7.8131
	validation	3.3192	4.4978	0.2234	7.8169
	testing	3.4481	4.6422	0.2309	8.0903
380 K	training	3.4135	4.6409	0.2119	8.0544
	validation	3.4127	4.6332	0.2156	8.0459
	testing	3.3035	4.4568	0.2265	7.7603
400 K	training	3.5046	4.7743	0.2067	8.2789
	validation	3.5152	4.7927	0.2073	8.3079
	testing	3.5246	4.8109	0.2198	8.3355

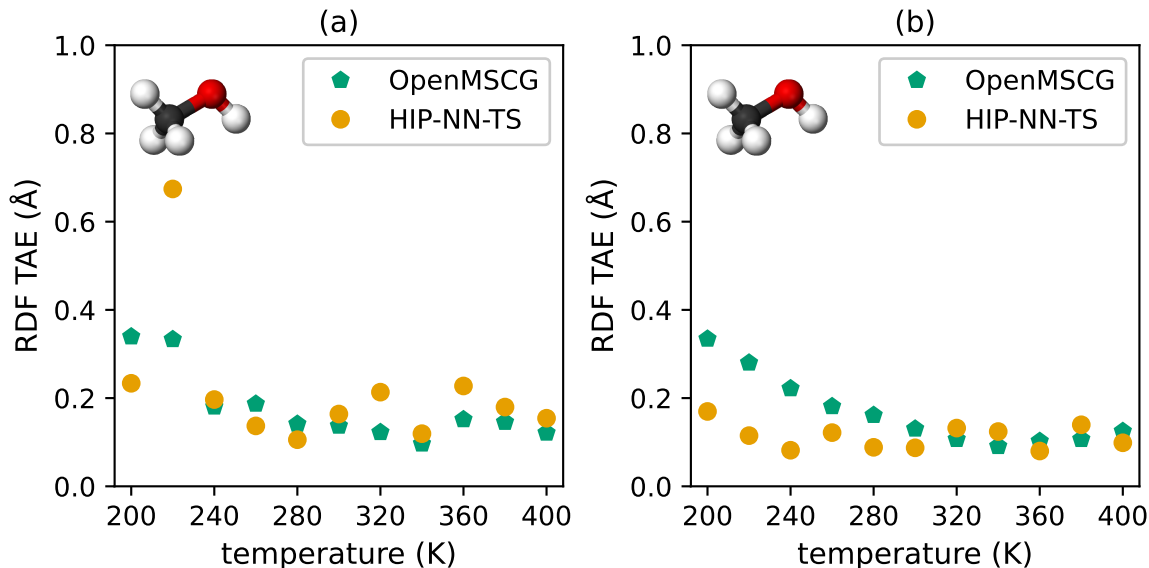


Figure S1: Results of the methanol comparison study where both the ML CG and OpenMSCG models were trained using (a) 10 and (b) 100 frames of training data.

Effects of training set size

We repeated the methods used in both the methanol comparison study and the cross-molecular study in the main text but with fewer frames in the ML CG and OpenMSCG model training data sets to investigate how the training data size affects the models' performance. The speed and automation of the developed workflows made training the 170+ additional ML CG models and running the 420+ additional MD runs needed for these analyses a feasible task.

Figure S1 shows the results for the methanol comparison study. In this investigation, both the OpenMSCG models and the ML CG models were trained using only 10 (subfigure (a)) and 100 (subfigure (b)) frames in the training data set, as opposed to the 1,000 frames used in the results discussed in the main text. For 10 frames, both methods exhibit errors within two times the errors (i.e. TAEs) of the original trial using 1,000 frames, with the exception of the ML CG model at 200 K, which has an error approximately four times the error for the 1,000 frames trial. Additionally, there is more fluctuation/noise in the results, indicating that the performance may be more sensitive to the random sample of training frames used.

For the trial using 100 frames of training data, this fluctuation is noticeably decreased. In fact, the OpenMSCG results are only narrowly distinguishable from the results for 1,000 frames. Some fluctuation is still apparent in the results of the ML CG models, although the errors are decreased in comparison with the 10 frame trial. These findings indicate that the performance of the OpenMSCG models may saturate earlier than the performance of the ML CG models, when provided access to more training data.

Figure S2 shows the results of the cross-molecular study when 100, rather than 1,000, frames of training data are used. In general, we observe higher error in some cases and a larger standard deviation (represented by the error bars) in many cases. For methanol (subfigure (a)), the errors are on average about a factor of two greater than the errors for the trial with 1,000 frames. The standard deviation of the errors is also 2-4 times greater in the highest density case, largely unchanged in the middle density case, and extremely large (up to 0.75 Å) in the lowest density case. Closer investigation revealed that the cause of the high error in the lowest density case was an effect resembling a phase change in some of the MD runs. For benzene, the differences between the 100 frame trial and the 1,000 frame trial are less pronounced. Errors up to twice the errors of the 1,000 frame trial are observed in the 100 frame trial, but in most instances, the change is much less. Additionally, the standard deviations are up to twice as high in the 100 frame case, but again, in most cases the difference is not this great. Most notable is that the standard deviation for the single-state models is noticeably higher, particularly in the highest density case. Finally, the results for methane are shown in subfigure (c). The results in the main text for the methane models trained on 1,000 frames of data were remarkably consistent with extremely low error and standard deviation. The results show here for the trial with 100 frames are nearly identical, with the most noticeable difference being a higher standard deviation on the multi-state model for the low-temperature, low-density case. While the results for the methanol models were significantly improved by the addition of more training data, the methane models exhibit little change. This suggests that the needed number of frames of

training data varies based on the geometry and/or size of the molecule.

Interpolation test

Figure S3 shows the results of an interpolation test for the multi-state ML CG model trained for methanol in the cross-molecular study. This multi-state model was trained with data generated at nine state points representing each combination of three temperatures—600 K, 700 K, and 800 K—and three densities—1.27 g/cm³, 1.03 g/cm³, and 0.85 g/cm³. The purpose of the test was to determine whether the model had simply learned how to perform at those nine state points or if it is able to extend its performance to intermediate state points (temperature between 600 K and 800 K and density between 1.27 g/cm³ and 0.85 g/cm³).

The four state points chosen for this test were at each combination of the temperatures 650 K and 750 K and densities 1.12 g/cm³ and 0.92 g/cm³. For each test state point, AA MD was run in the same manner used to generate training data as described in the Training subsection of the main text. This AA data was not used for model training, however, but solely to generate AA RDFs. Randomly selected frames from the AA trajectories were also used as initial starting points for the CG MD. The RDFs generated from running CG MD using the methanol multi-state model are also shown in the figure. The resulting TAEs range from 0.10 Å to 0.25 Å, perfectly in line with the results for the state points represented in the model training data which ranged from about 0.10 Å to about 0.45 Å. The general trend of the methanol multi-state model performing slightly better at lower temperatures, which was observed in analysis of the cross-molecular study results in the main text, can also be seen clearly here. Based on these findings, we expect that the multi-state model would perform similarly well on any state points within the range of the model training data, with slightly better results at lower temperatures.

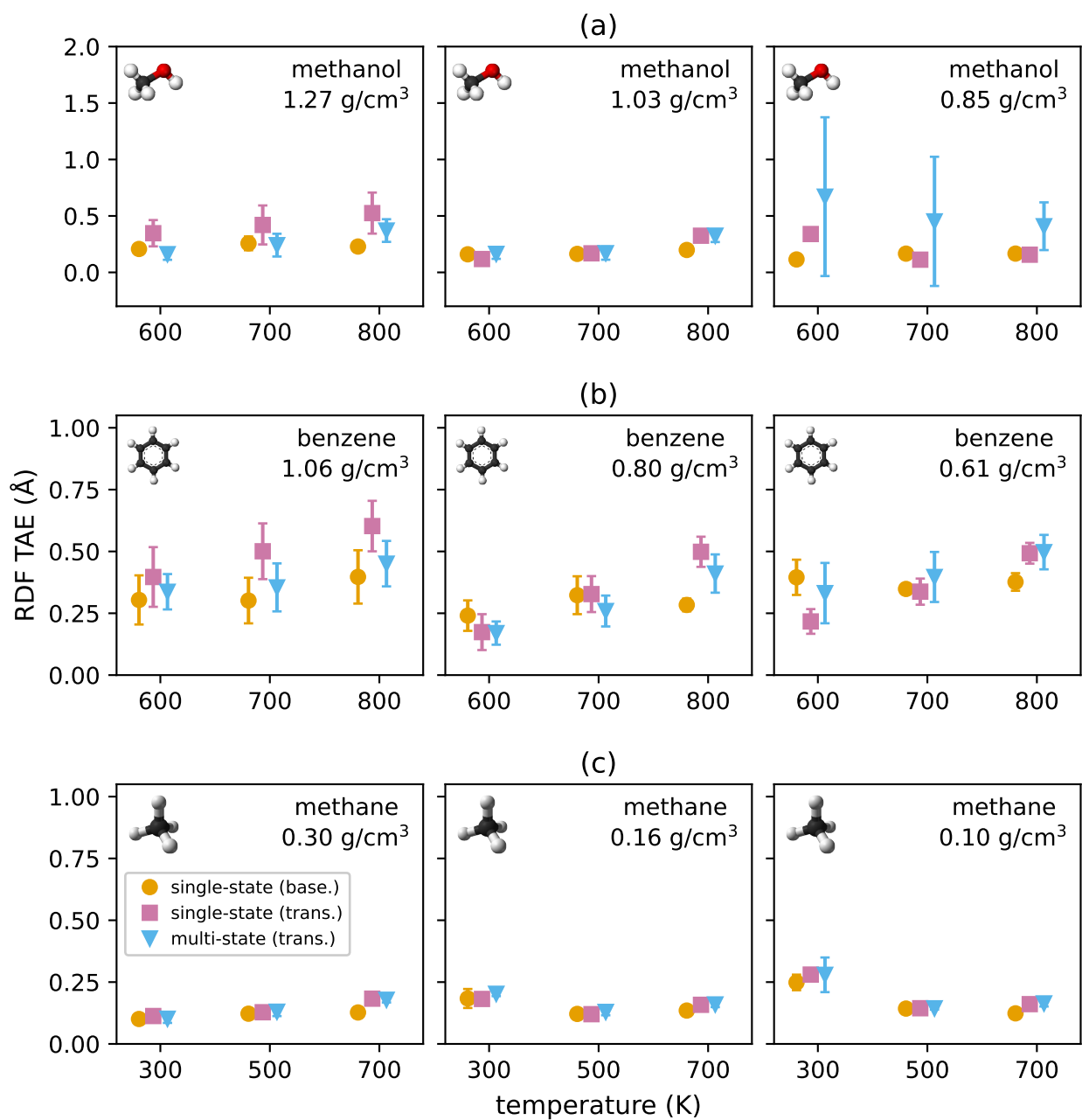


Figure S2: Results of the cross-molecular study when 100 frames rather than 1000 frames were used to train the various models for (a) methanol, (b) benzene, and (c) methane. Notice that the vertical scale on the methanol plot differs from that of the other two plots.

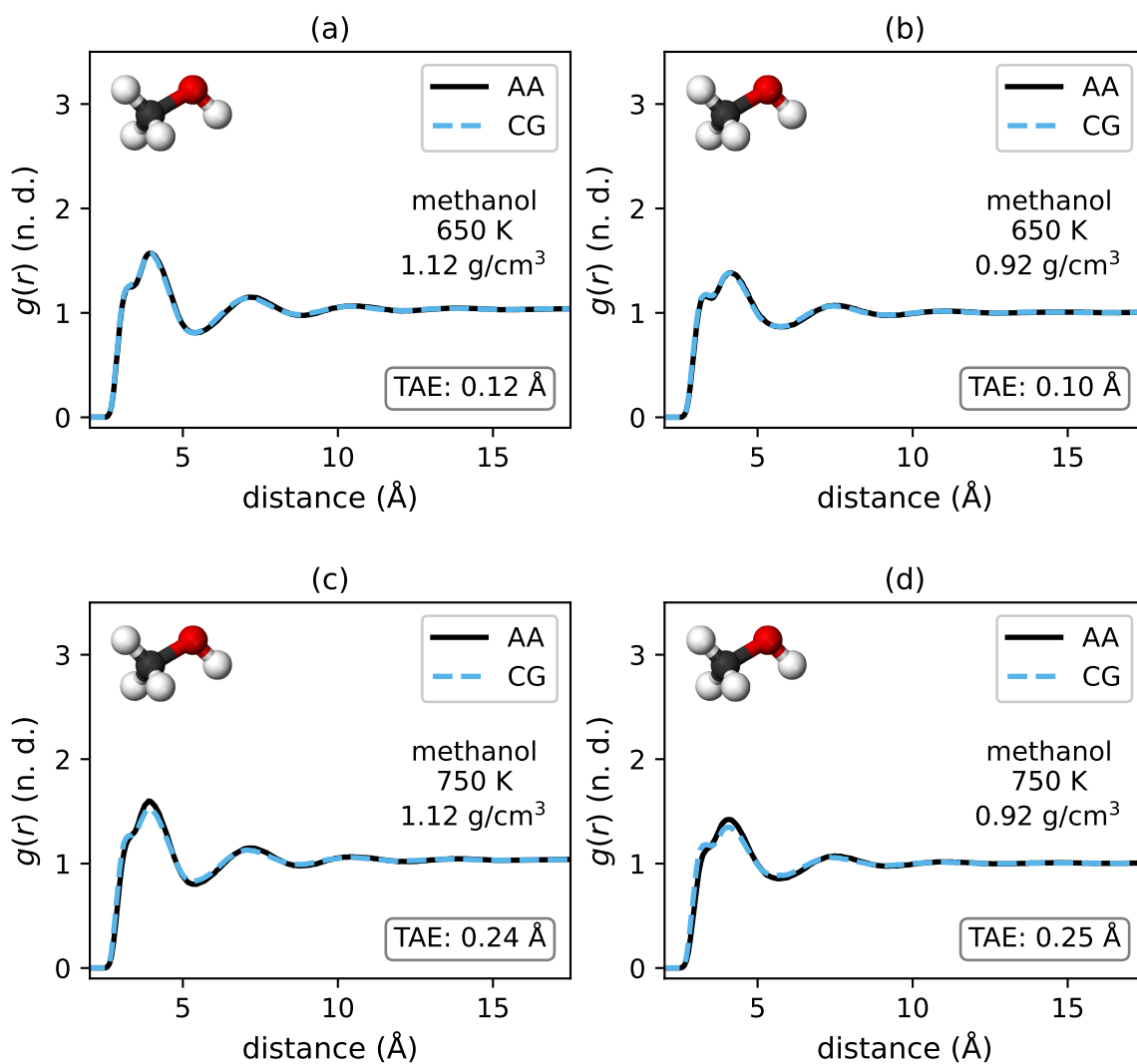


Figure S3: RDFs generated with AA MD compared with the multi-state ML CG models for methanol. The temperatures and densities at which these RDFs were generated were not included in the training data for the multi-state model.